BRIEF DEFINITIVE REPORT

ApoE facilitates the microglial response to amyloid plaque pathology

Jason D. Ulrich[1,2,3]*, Tyler K. Ulland[4]*, Thomas E. Mahan[1,2,3]*, Sofie Nyström[5], K. Peter Nilsson[5], Wilbur M. Song[4], Yingyue Zhou[4], Mariska Reinartz[1,6], Seulah Choi[1,2,3], Hong Jiang[1,2,3], Floy R. Stewart[1,2,3], Elise Anderson[1,2,3], Yaming Wang[4,7], Marco Colonna[4], and David M. Holtzman[1,2,3]

One of the hallmarks of Alzheimer's disease is the presence of extracellular diffuse and fibrillar plaques predominantly consisting of the amyloid-β (Aβ) peptide. Apolipoprotein E (ApoE) influences the deposition of amyloid pathology through affecting the clearance and aggregation of monomeric Aβ in the brain. In addition to influencing Aβ metabolism, increasing evidence suggests that apoE influences microglial function in neurodegenerative diseases. Here, we characterize the impact that apoE has on amyloid pathology and the innate immune response in APPPS1ΔE9 and APPPS1-21 transgenic mice. We report that *Apoe* deficiency reduced fibrillar plaque deposition, consistent with previous studies. However, fibrillar plaques in *Apoe*-deficient mice exhibited a striking reduction in plaque compaction. Hyperspectral fluorescent imaging using luminescent conjugated oligothiophenes identified distinct Aβ morphotypes in *Apoe*-deficient mice. We also observed a significant reduction in fibrillar plaque–associated microgliosis and activated microglial gene expression in *Apoe*-deficient mice, along with significant increases in dystrophic neurites around fibrillar plaques. Our results suggest that apoE is critical in stimulating the innate immune response to amyloid pathology.

Introduction

One of the hallmark pathologies of Alzheimer's disease (AD) is the presence of extracellular deposits of diffuse and fibrillar amyloid plaques predominantly consisting of the amyloid-β (Aβ) peptide. Aβ-related pathology is accompanied by the clustering of microglia around fibrillar plaques, although the molecular mechanisms facilitating microglial clustering are still poorly understood (Aguzzi et al., 2013). The formation of Aβ plaques within the brain parenchyma is influenced by the concentration of monomeric forms of Aβ in the interstitial fluid and by other proteins in the brain, perhaps most notably apolipoprotein E (apoE; Musiek and Holtzman, 2015). ApoE has previously been shown to influence the rate of monomeric Aβ clearance from the brain interstitial fluid in an isoform-dependent manner and to influence the kinetics of amyloid formation in vitro (Bell et al., 2007; Deane et al., 2008; Huynh et al., 2017a). Both of these characteristics likely contribute to apoE-dependent effects on Aβ plaque formation in vivo.

In addition to influencing Aβ metabolism, increasing evidence suggests that apoE may influence the microglial response

in different ways in the context of neurodegenerative disease. ApoE is predominantly expressed by astrocytes but it is strongly up-regulated by microglia in the context of Aβ pathology and can influence the activation state of microglia (Uchihara et al., 1995; Butovsky et al., 2015; Krasemann et al., 2017). The role of microglia in the course of AD remains ambiguous. Recent genetic evidence strongly implicates microglial function in playing a critical role in the disease. Variants in microglial-expressed genes, such as *TREM2* and *CD33* alter the risk of developing AD, implicating the importance of microglia in the onset and progression of AD (Naj et al., 2011; Griciuc et al., 2013; Guerreiro et al., 2013; Jonsson et al., 2013). Although chronic microglial activation is hypothesized to result in neurotoxic inflammatory signaling, recent studies have shown that plaque-associated microgliosis was negatively correlated with the degree of neuritic dystrophy around plaques, suggesting a potential protective role for microglia in response to amyloid plaque formation (Condello et al., 2015; Heneka et al., 2015). Mouse models of Aβ deposition that are haploinsufficient or completely deficient in *Trem2* exhibit

[1]Department of Neurology, Washington University School of Medicine, St. Louis, MO; [2]Knight Alzheimer's Disease Research Center, Washington University School of Medicine, St. Louis, MO; [3]Hope Center for Neurological Disorders, Washington University School of Medicine, St. Louis, MO; [4]Department of Pathology and Immunology, Washington University School of Medicine, St. Louis, MO; [5]Department of Chemistry, IFM, Linköping University, Linköping, Sweden; [6]Radboud University Nijmegen, Nijmegen, Netherlands; [7]Eli Lilly and Company, Lilly Corporate Center, Indianapolis, IN.

*J.D. Ulrich, T.K. Ulland, and T.E. Mahan contributed equally to this paper; Correspondence to Marco Colonna: mcolonna@pathology.wustl.edu; David M. Holtzman: holtzman@neuro.wustl.edu.

reduced plaque-associated microgliosis, and *Trem2*-deficient mice exhibit altered plaque morphology and increased neuritic dystrophy, suggestive of a role for microglia in shaping the gross structure of plaques and reducing plaque-associated toxicity (Ulrich et al., 2014; Wang et al., 2015, 2016; Yuan et al., 2016; Jay et al., 2017; Song et al., 2017; Ulland et al., 2017).

Previous studies found that genetic deletion of *Apoe* in amyloid-depositing mouse models overexpressing human amyloid precursor protein (APP), but not PS1, resulted in a dramatic decrease in diffuse plaques and an absence of fibrillar plaque formation (Bales et al., 1997; Holtzman et al., 1999, 2000). However, more recently developed aggressive mouse models of amyloid deposition exhibit modest fibrillar amyloid deposition in the absence of apoE (Katsouri and Georgopoulos, 2011). The effect of the lack of *Apoe* expression in these mouse models on the tissue response to amyloid pathology is not currently understood and provides an opportunity to understand the role of apoE in this process. In this study, we characterize the impact that apoE has on amyloid pathology and the innate immune response in both the APPPS1ΔE9 and APPPS1-21 amyloid-developing mouse models. We found that *Apoe*-deficient mice exhibited reduced fibrillar plaque deposition and altered regional distribution of plaque pathology within the hippocampus, consistent with previous studies (Holtzman et al., 1999; Irizarry et al., 2000; Fagan et al., 2002). However, fibrillar plaques in *Apoe*-deficient mice exhibited a striking reduction in plaque compaction, and hyperspectral fluorescent imaging using luminescent conjugated oligothiophenes (LCOs) identified distinct Aβ morphotypes in *Apoe*-deficient mice. We also observed a significant reduction in plaque-associated microgliosis and activated microglial gene expression in *Apoe*-deficient mice, along with significant increases in dystrophic neurites. Our results suggest that apart from influencing Aβ plaque formation, apoE facilitates plaque-associated microgliosis and limits plaque-associated neuronal toxicity.

Results and discussion

ApoE modifies Aβ deposition

Previous studies in human APP transgenic mice, PDAPP and Tg2576, found that *Apoe* deficiency significantly reduced both total and fibrillar Aβ deposition (Bales et al., 1997, 1999; Holtzman et al., 2000; Irizarry et al., 2000). Therefore, we first assessed total Aβ deposition in the cortex and hippocampus of 6-mo-old APPPS1 and *Apoe*⁻/⁻;APPPS1 mice using an N-terminal Aβ antibody. Surprisingly, we observed significantly more Aβ deposition in the cortex of *Apoe*⁻/⁻;APPPS1 compared with APPPS1 mice, which was attributable to a significant increase in both the number and size of cortical Aβ immunostained plaques in the absence of *Apoe* expression (Fig. 1, A–D). Marked cortical Aβ deposition was also observed in 10-mo-old *Apoe*⁻/⁻;APPPS1ΔE9 mice (Fig. 1 E). The overall cortical plaque burden did not significantly differ between APPPS1ΔE9 and *Apoe*⁻/⁻;APPPS1ΔE9 mice; however, there was a significant decrease in the number of Aβ plaques (Fig. 1, F and G). Interestingly, the average size of Aβ plaques was significantly larger in *Apoe*⁻/⁻;APPPS1ΔE9 mice than in APPPS1ΔE9 mice, consistent with the effect of apoE on plaque

size in the APPPS1 model (Fig. 1 H). In agreement with previous studies (Bales et al., 1997; Holtzman et al., 2000), we observed a marked shift in the regional distribution of Aβ plaques within the hippocampus from the molecular layer of the dentate gyrus to the hilus (Fig. 1, A and E).

In previous studies, Tg2576 and PDAPP mice deficient in *Apoe* exhibited virtually no true fibrillar amyloid, suggesting that apoE is necessary for Aβ to form Aβ containing a β-sheet structure, i.e., amyloid (Bales et al., 1997; Holtzman et al., 2000). Given that we observed significant levels of Aβ plaque pathology in both APPPS1 and APPPS1ΔE9 mice in the absence of *Apoe*, we decided to assess whether the fibrillar amyloid burden was significantly altered by *Apoe* deficiency using X-34, which labels amyloid structures (Styren et al., 2000). The cortical and hippocampal amyloid burden in both 6-mo-old *Apoe*⁻/⁻;APPPS1 and *Apoe*⁻/⁻;APPPS1ΔE9 mice was strongly reduced in the absence of apoE compared with mice expressing *Apoe*; however, fibrillar plaques were detectable in the absence of *Apoe* expression in both strains (Fig. 1, I–N). Biochemical analysis of cortical tissue from 6-mo-old APPPS1 and *Apoe*⁻/⁻;APPPS1 mice revealed decreased levels of insoluble Aβ$_{40}$ and Aβ$_{42}$, consistent with the observed decrease in X-34⁺ plaque pathology (Fig. S1 A). Interestingly, although soluble Aβ$_{40}$ levels were decreased in *Apoe*⁻/⁻;APPPS1 mice, soluble Aβ$_{42}$ levels were slightly but statistically significantly elevated (Fig. S1 B). This might reflect the increase in diffuse Aβ pathology observed by N-terminal Aβ antibody staining (Fig. 1 A). Western blot analysis of APP and the APP C99 cleavage fragment did not reveal a significant difference in the ratio of C99 to APP, suggesting that apoE did not significantly affect APP processing by β-secretase (Fig. S1, C and D).

Recent studies indicate that apoE expression influences the initiation of fibrillar plaque deposition, but not the subsequent growth of amyloid plaques once plaque formation has occurred (Huynh et al., 2017b; Liu et al., 2017). This would suggest that apoE serves as a catalyst for the folding of Aβ peptides into higher-order amyloid/β-sheet conformations. Aβ$_{42}$ exhibits a greater propensity to form amyloid fibrils, and variants in *APP*, *PSEN1*, or *PSEN2* that increase the production of Aβ$_{42}$ relative to shorter Aβ species result in autosomal dominant AD (Musiek and Holtzman, 2015). We speculate that the differences we report here in *Apoe*-deficient APPPS1 models compared with earlier APP overexpression models stems largely from differences in the relative production of Aβ$_{42}$:Aβ$_{40}$ in these different strains. Tg2576 mice exhibited a roughly 1:5 ratio of Aβ$_{42}$/Aβ$_{40}$ in young animals, compared with an ~1:1 ratio in APPPS1 and APPPS1ΔE9 mice, which likely results in the accelerated development of Aβ-deposition in APPPS1 and APPPS1ΔE9 mice and the formation of amyloid (Jankowsky et al., 2004; Radde et al., 2006). Thus, although apoE may catalyze the conversion of Aβ into a fibrillar state, high relative generation of Aβ$_{42}$ may be sufficient for the development of some true amyloid even in the absence of apoE.

ApoE regulates amyloid morphology and conformation

We noted that the amyloid plaques in *Apoe*⁻/⁻ mice appeared to not stain as intensely with X-34 as in *Apoe*⁺/⁺ mice. Given that the plaques in *Apoe*⁻/⁻;APPPS1 plaques were larger than plaques in APPPS1 mice, we decided to assess the effect of ApoE on plaque
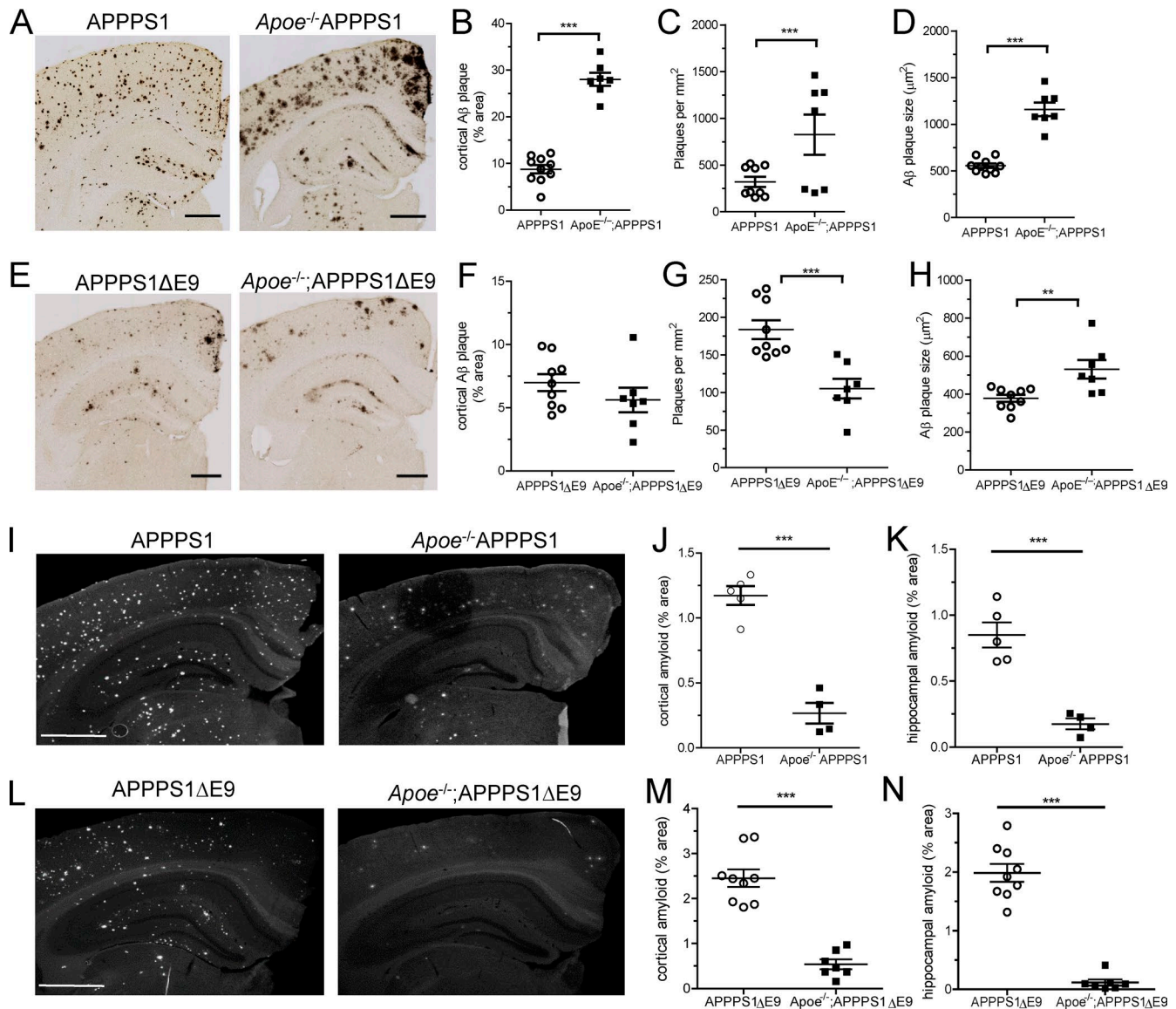
Ulrich et al.
ApoE and microglia activation in amyloid models

Journal of Experimental Medicine 1048
https://doi.org/10.1084/jem.20171265

Figure 1. **Apoe deficiency increases Aβ plaque size but decreases amyloid burden. (A)** Representative images of APPPS1 and *Apoe*−/−;APPPS1 mice stained with an N-terminal Aβ antibody. **(B)** The percentage of cortical area immunopositive for Aβ was increased in *Apoe*−/−;APPPS1 mice (28.0 ± 1.4%, *n* = 7 mice) relative to APPPS1 (8.8 ± 0.9%, *n* = 10 mice); t(15) = 12.1, P < 0.0001, Student's *t* test. **(C)** The mean number of plaques was increased in *Apoe*−/−;APPPS1 mice (230.6 ± 6.5, *n* = 7 mice) relative to APPPS1 (172.8 ± 9.6, *n* = 9); t(14) = 4.7, P = 0.0003. **(D)** The mean plaque size was increased in *Apoe*−/−;APPPS1 mice (1,159 ± 72.9 μm², *n* = 7 mice) relative to APPPS1 (555.1 ± 23.2 μm², *n* = 10); t(15) = 9.1, P < 0.0001, Student's *t* test. **(E)** Representative images of APPPS1ΔE9 and *Apoe*−/−;APPPS1ΔE9 mice stained with an N-terminal Aβ antibody. **(F)** The percentage of cortical area immunopositive for Aβ was not significantly different between APPPS1ΔE9 (7.0 ± 0.7%, *n* = 9 mice) and *Apoe*−/−;APPPS1ΔE9 (5.6 ± 1.0%, *n* = 7 mice); t(14) = 1.2, P = 0.25, Student's *t* test. **(G)** The number of cortical plaques was significantly reduced in *Apoe*−/−;APPPS1ΔE9 mice (105.2 ± 13.0, *n* = 7 mice) compared with APPPS1ΔE9 mice (183.5 ± 12.4, *n* = 9 mice); t(14) = 4.3, P = 0.0007, Student's *t* test. **(H)** The mean plaque size was increased in *Apoe*−/−;APPPS1ΔE9 mice (529.8 ± 48.6 μm², *n* = 7 mice) compared with APPPS1ΔE9 mice (377.9 ± 18.5 μm², *n* = 9 mice); t(14) = 3.2, P = 0.0064, Student's *t* test. **(I)** Representative images of APPPS1 and *Apoe*−/−;APPPS1 mice stained with X-34. **(J)** The percentage of cortical area stained with X-34 was significantly decreased in *Apoe*−/−;APPPS1 mice (0.27 ± 0.08, *n* = 5 mice) compared with APPPS1 (1.2 ± 0.07, *n* = 4 mice); t(7) = 8.411, P < 0.0001, Student's *t* test. **(K)** The percentage of hippocampal area stained with X-34 was significantly decreased in *Apoe*−/−;APPPS1 mice (0.18 ± 0.04, *n* = 4 mice) compared with APPPS1 (0.85 ± 0.1, *n* = 5 mice); t(7) = 5.9, P = 0.0006, Student's *t* test. **(L)** Representative images of APPPS1ΔE9 and *Apoe*−/−;APPPS1ΔE9 mice stained with X-34. **(M)** The percentage of cortical area stained with X-34 was significantly decreased in *Apoe*−/−;APPPS1ΔE9 mice (0.54 ± 0.11%, *n* = 7 mice) compared with APPPS1ΔE9 (2.5 ± 0.19%, *n* = 9 mice); t(14) = 8.0, P < 0.0001, Student's *t* test. **(N)** The percentage of hippocampal area stained with X-34 was significantly decreased in *Apoe*−/−;APPPS1ΔE9 mice (0.12 ± 0.05%, *n* = 7 mice) compared with APPPS1ΔE9 (2.0 ± 0.15, *n* = 9 mice); t(14) = 10.4, P < 0.0001, Student's *t* test. All values given and plotted as mean ± SEM. Bars, 500 μm. **, P < 0.01; ***, P < 0.001.

morphology. High-resolution confocal imaging of amyloid plaques revealed that the gross morphology of the plaque was strikingly different in the presence and absence of apoE (Fig. 2 A). Amyloid plaques in 6-mo-old APPPS1 and 10-mo-old APPPS1ΔE9 mice had a distinct, dense core that was intensely stained with X-34 (Fig. 2 A). In contrast, plaques in *Apoe*−/−;APPPS1 and *Apoe*−/−; APPPS1ΔE9 mice contained numerous wispy fibrils, projecting out from a loosely defined core (Fig. 2 A). We quantitatively assessed
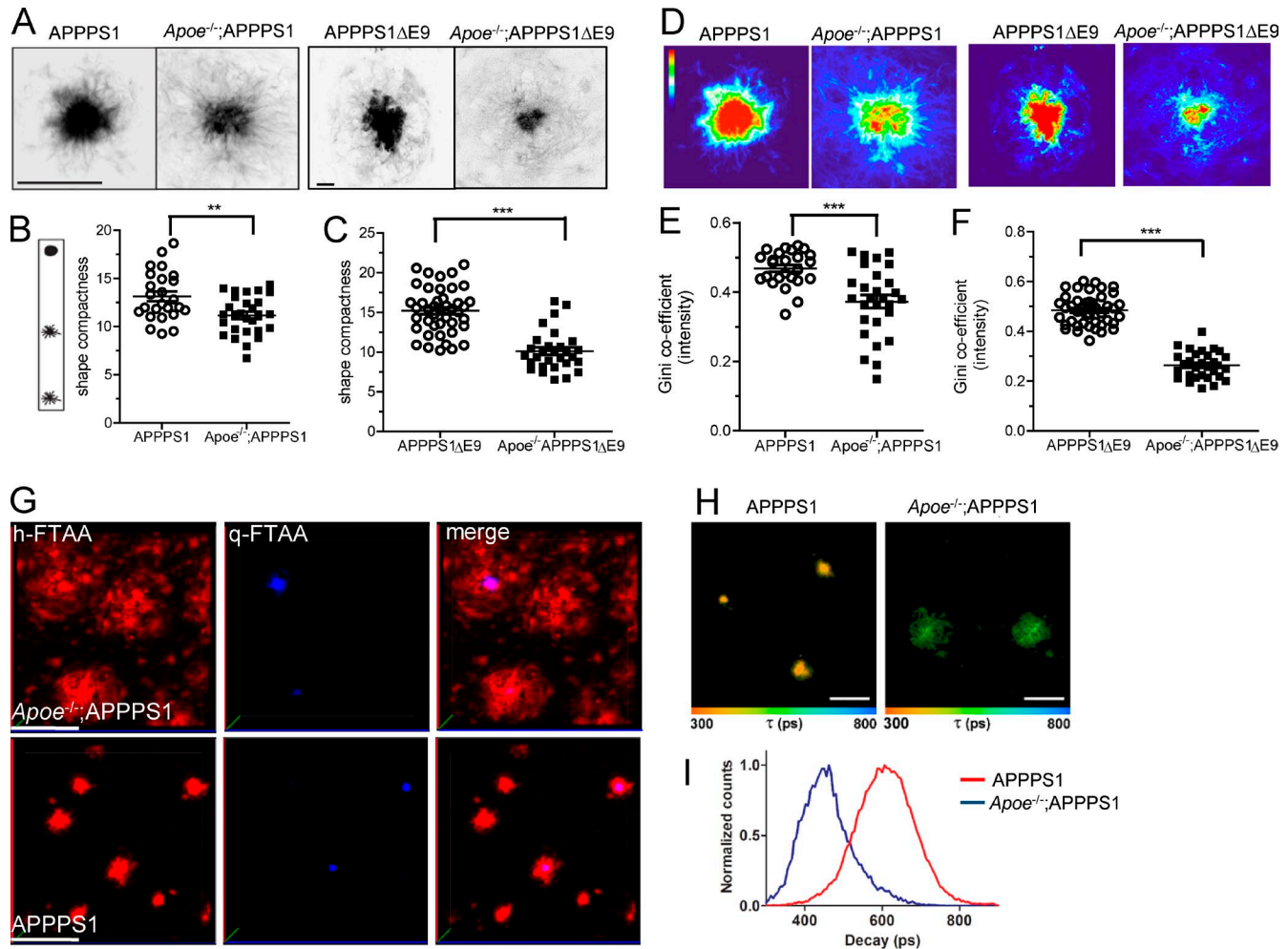
Figure 2. **Apoe deficiency alters amyloid morphology and conformation. (A)** Representative, high-magnification images of X-34+ plaques from APPPS1 and *Apoe*−/−;APPPS1 mice and APPPS1ΔE9 and *Apoe*−/−;APPPS1ΔE9 mice. Bars, 10 µm. **(B)** Significant decrease in the shape compactness of *Apoe*−/−;APPPS1 mice (11.18 ± 0.38, *n* = 28 plaques) compared with APPPS1 (13.14 ± 0.50, *n* = 25 plaques); t(51) = 3.2, P < 0.001, Student's *t* test. **(C)** Significant decrease in the shape compactness of *Apoe*−/−;APPPS1ΔE9 (10.12 ± 0.47, *n* = 29 plaques) compared with APPPS1ΔE9 (15.19 ± 0.44, *n* = 43 plaques); t(70) = 7.6, P < 0.001, Student's *t* test. **(D)** Representative pixel intensity heat maps for APPPS1 and *Apoe*−/−;APPPS1. Same scale bars as in A. **(E and F)** The Gini coefficient for pixel intensity was decreased in *Apoe*−/−;APPPS1 mice (0.37 ± 0.02, *n* = 28 plaques) compared with APPPS1 (0.47 ± 0.01, *n* = 25 plaques); t(51) = 4.3, P < 0.0001, Student's *t* test (E) and the Gini coefficient for *Apoe*−/−;APPPS1ΔE9 mice (0.26 ± 0.01, *n* = 29) compared with APPPS1ΔE9 (0.48 ± 0.01, *n* = 43 plaques); t(70) = 15.53, P < 0.0001, Student's *t* test (F). Values are given and plotted as mean ± SEM. **(G)** Fluorescence images of Aβ-deposits costained by the tetrameric LCO, q-FTAA (blue), and the heptameric LCO, h-FTAA (red). The images are rendered from z-stacks recorded with the dimensions of x = 250 µm (red line), y = 250 µm (blue line), and z = 90 µm (green line; bar, 75 µm). **(H and I)** Fluorescence lifetime images (H) and lifetime decay curves (I) for h-FTAA stained Aβ-deposits in brain tissue sections. The color bar represents lifetimes from 300 ps (orange) to 800 ps (blue) and the images are color-coded according to the representative lifetime. The fluorescence lifetimes were collected with excitation at 490 nm. Fluorescence decays were collected from 5 to 10 different plaques in tissue sections from five individual APPPS1- or *Apoe*−/−;APPPS1 mice. Bars, 20 µm. **, P < 0.01; ***, P < 0.001.

these qualitative observations using a shape compactness index that takes into account the perimeter and two-dimensional area of the plaque and found that *Apoe*−/−;APPPS1 and *Apoe*−/−;APPPS1ΔE9 mice exhibited a significantly less compact morphology (Fig. 2, B and C). We further quantitatively compared plaques by assessing the Gini coefficient of pixel intensity for X-34 staining (Fig. 2, D–F). We found that plaques from *Apoe*−/−;APPPS1 and *Apoe*−/−;APPPS1ΔE9 mice exhibited a significant decrease in the Gini coefficient, consistent with the observed decrease in intensity of the dense X-34+ core of amyloid plaques compared with APPPS1 and APPPS1ΔE9 mice (Fig. 2, E and F).

A previous study demonstrated that a combination of two LCOs, q-FTAA and h-FTAA, can be used for spectral assignment of distinct aggregated Aβ morphotypes (Nyström et al., 2013). q-FTAA stains only mature fibrillar Aβ deposits that are also recognized by conventional amyloid ligands, such as thioflavin T and X-34, whereas h-FTAA detects a broader subset of disease-associated protein aggregates (Klingstedt et al., 2011, 2013; Nyström et al., 2013; Magnusson et al., 2014). Given the stark contrast in amyloid plaque morphology in *Apoe*−/− mice, we stained tissue sections from 6-mo-old *Apoe*−/−;APPPS1 and APPPS1 mice with a mixture of q-FTAA and h-FTAA. Hyperspectral fluorescence imaging revealed distinct staining patterns using q-FTAA and h-FTAA dependent on the *Apoe* genotype. For all mice, minor q-FTAA fluorescence was only observed in the core of some plaques. In contrast, h-FTAA staining was

Ulrich et al.
ApoE and microglia activation in amyloid models

Journal of Experimental Medicine
https://doi.org/10.1084/jem.20171265

1050

much more abundant in the *Apoe*⁻ᐟ⁻;APPPS1 mice compared with APPPS1 mice (Fig. 2 G). Hence, in accordance with anti-Aβ antibody staining, h-FTAA fluorescence displayed a greater amount of Aβ deposition in mice lacking *Apoe*, and these deposits are most likely composed of an Aβ morphotype that is only detected by h-FTAA.

To examine the difference in Aβ morphotypes further, we performed fluorescence-lifetime imaging (FLIM) analysis of h-FTAA–stained Aβ deposits. FLIM is a powerful technique that can be used to determine both differential states of binding and to observe minute variations in ligand–aggregate interactions, and differences in fluorescence decays from h-FTAA have previously been observed from the ligand bound to prion aggregates associated with specific prion strains (Magnusson et al., 2014). For APPPS1 mice, h-FTAA–stained Aβ deposits displayed fluorescence decays between 350–600 ps, whereas the decays from h-FTAA bound to Aβ deposits in *Apoe*⁻ᐟ⁻;APPPS1 mice were considerably longer at 400–800 ps (Fig. 2, H and I). Hence, a distinct distribution of fluorescence decays was observed for h-FTAA depending on the *Apoe* genotype, suggesting that the lack of apoE induces an enrichment of a specific Aβ morphotype.

Decreased plaque-associated microgliosis and activated microglial gene expression in *Apoe*⁻ᐟ⁻;APPPS1 and *Apoe*⁻ᐟ⁻;APPPS1ΔE9 mice

Apoe expression is up-regulated in response to amyloid pathology and is thought to play a role in the innate immune response in the central nervous system. Interestingly, lipidated apoE binds to TREM2 in vitro and may be a potential physiological ligand mediating TREM2 activation (Atagi et al., 2015; Yeh et al., 2016). Given that a lack of *Trem2* expression impairs plaque-associated microgliosis, we decided to test whether a lack of *Apoe* expression affected the microglial response to amyloid plaques. As expected, both 6-mo-old APPPS1 and 10-mo-old APPPS1ΔE9 mice exhibited pronounced microglial clustering around amyloid plaques (Fig. 3, A and C). However, the number of microglia located within 15 or 30 µm of a plaque was significantly decreased in both *Apoe*⁻ᐟ⁻;APPPS1 and *Apoe*⁻ᐟ⁻;APPPS1ΔE9 mice (Fig. 3, A–D). The number of microglia located farther than 30 µm from a plaque were unaffected by *Apoe* genotype, suggesting that the effect of apoE on microglial function was specific to activated microglia around amyloid plaques (Fig. 3, B and D).

To further assess the effect of *Apoe* deficiency in the context of amyloid pathology, we performed RNA sequencing (RNAseq) analysis on cortical tissue from 6-mo-old APPPS1 and *Apoe*⁻ᐟ⁻;APPPS1 mice. Gene-level analysis revealed that 115 genes were differentially expressed in APPPS1 and *Apoe*⁻ᐟ⁻;APPPS1 mice (Fig. 3 E; Table S1). Changes in microglial gene expression in amyloid models detected using whole tissue methods may result from either the up-regulation of a given transcript at the cellular level or an increase in microglial abundance, which, in general, positively correlates with amyloid burden (Srinivasan et al., 2016). Evidence from single-cell RNAseq studies indicates that activated microglia around plaques, termed disease-associated microglia, exhibit up-regulation of several genes associated with lipid metabolism and phagocytosis, including *Itgax* and *Cst7*, which are significantly down-regulated in *Apoe*⁻ᐟ⁻;APPPS1

mice, consistent with a decrease in plaque-associated microgliosis (Fig. 3 G; Table S1; Keren-Shaul et al., 2017). Gene ontology analysis of differentially expressed genes found a significant enrichment in genes related to the immune system (Table S2), of which the vast majority were down-regulated (Fig. 3 E; Table S1). We further analyzed cytokine levels at the protein level in the hippocampus of 6-mo-old APPPS1 and *Apoe*⁻ᐟ⁻;APPPS1 mice and observed reduced levels of CCL3, consistent with the reduction in CCL3 transcript observed by RNAseq (Fig. 3 F). Interestingly there was a trend toward elevated TNFα in *Apoe*⁻ᐟ⁻;APPPS1 mice (Fig. 3 F). This may be attributable to increases in peripheral TNF-α expression in *Apoe*⁻ᐟ⁻ mice, since TNF-α is transported across the blood–brain barrier (BBB; Gutierrez et al., 1993; Grainger et al., 2004). Collectively, these data suggest an overall impairment in the microglial response to amyloid pathology in *Apoe*⁻ᐟ⁻ mice.

Increased neuritic dystrophy in *Apoe*⁻ᐟ⁻;APPPS1 mice

Emerging data suggest that reductions in plaque-associated microgliosis are associated with increases in dystrophic neurites around plaques (Condello et al., 2015; Wang et al., 2016; Yuan et al., 2016). Previous studies reported a lack of dystrophic neurites in *Apoe*⁻ᐟ⁻ mice crossed with either the PDAPP or Tg2576 models (Holtzman et al., 2000). However, as noted above, PDAPP and Tg2576 mice developed minimal, if any, fibrillar plaques in the absence of apoE. Moreover, accumulations of protofibrillar Aβ species within amyloid plaques are spatially associated with increases in dystrophic neurites (Condello et al., 2015). Since the *Apoe*⁻ᐟ⁻;APPPS1 and *Apoe*⁻ᐟ⁻;APPPS1ΔE9 mice developed significant fibrillar and diffuse plaques, and exhibit significant reductions in microgliosis, we tested whether these mice exhibited any differences in plaque-associated neuronal toxicity. We labeled dystrophic neurites with an N-terminal APP antibody (NT-APP) and quantified the abundance of NT-APP staining within 30 µm of a plaque. (Fig. 4, A and C). The number of dystrophic neurites around plaques was significantly increased in both 6-mo-old *Apoe*⁻ᐟ⁻;APPPS1 and 10-mo-old *Apoe*⁻ᐟ⁻;APPPS1ΔE9 (Fig. 4, B and D). This observation is consistent with a role for apoE in facilitating plaque-associated microgliosis and reducing plaque-associated neuronal damage.

Final comments and conclusion

Considerable evidence suggests that apoE influences the propensity of Aβ to aggregate into fibrillar plaques through several potential mechanisms, including affecting the rate of Aβ clearance from the brain and the rate of conversion of Aβ monomers and oligomers to mature fibrils (Huynh et al., 2017a). However, beyond its effect on amyloid, apoE also influences diverse processes in the brain, such as synaptogenesis, phagocytosis, BBB function, and microglial activation (Mauch et al., 2001; Bell et al., 2012; Butovsky et al., 2015; Chung et al., 2016; Krasemann et al., 2017; Shi et al., 2017). The histological and gene expression data presented in this study suggest that apoE not only affects the structure and level of amyloid pathology, but also the innate immune response to amyloid plaques, which in turn may protect against plaque-associated neurotoxicity. This observation supports a role for apoE downstream of plaque-deposition in regulating the toxicity and immune response to amyloid pathology.
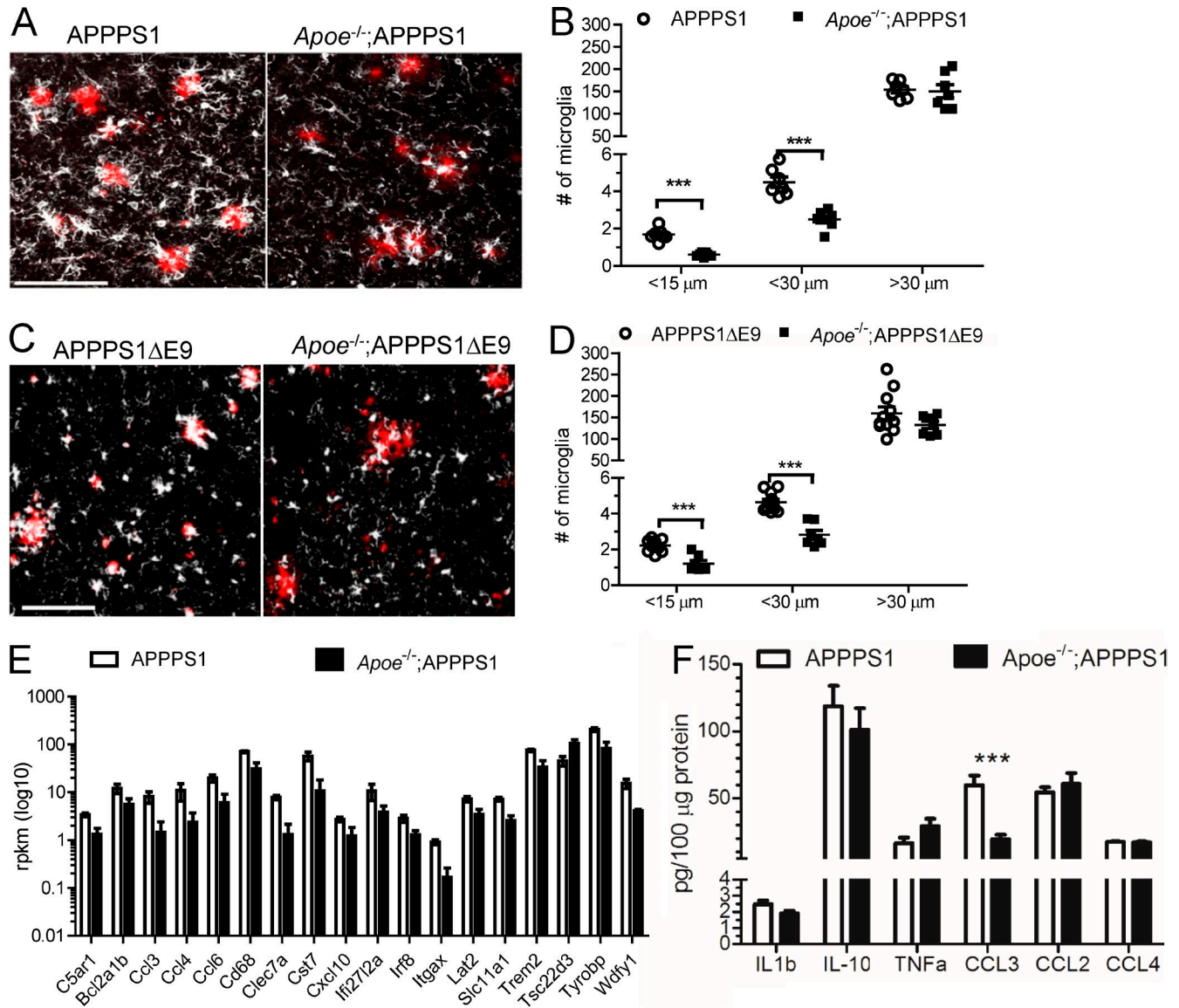
Ulrich et al.
ApoE and microglia activation in amyloid models

Journal of Experimental Medicine 1051
https://doi.org/10.1084/jem.20171265

Figure 3. **Decreased plaque-associated microgliosis in *Apoe*-deficient mice. (A)** Representative images of APPPS1 and *Apoe*−/−;APPPS1 mice stained with Iba1 to label microglia and X-34 to label amyloid plaques. **(B)** Significant reduction in the number of microglia in *Apoe*−/−;APPPS1 (0.60 ± 0.04, *n* = 7 mice) mice compared with APPPS1 (1.7 ± 0.12, *n* = 7) within 15 μm (t[12] = 8.3, P < 0.0001) and 30 μm (2.5 ± 0.18, *n* = 7 mice versus 4.5 ± 0.28, *n* = 7 mice); t(12) = 5.9, P < 0.0001, Student's *t* test. The number of microglia >30 μm from a plaque in APPPS1 (154.3 ± 7.1, *n* = 7 mice) compared with *Apoe*−/−;APPPS1 (150.7 ± 14.9, *n* = 7 mice) was not significantly different; t(12) = 0.22, P = 0.83, Student's *t* test. **(C)** Representative images of APPPS1ΔE9 and *Apoe*−/−;APPPS1ΔE9 mice stained with Iba1 and X-34. **(D)** Significant reduction in the number of microglia within 15 μm of *Apoe*−/−;APPPS1ΔE9 (1.2 ± 0.17, *n* = 7 mice), compared with APPPS1ΔE9 (2.2 ± 0.1, *n* = 11 mice); t(16) =5.6, P < 0.0001, Student's *t* test, and within 30 μm (2.8 ± 0.24, *n* = 7 mice) compared with (4.6 ± 0.16, *n* = 11 mice); t(16) = 6.5, P < 0.0001, Student's *t* test. The number of microglia >30 μm from a plaque in APPPS1ΔE9 (160.3 ± 14.7, *n* = 11 mice) and *Apoe*−/−;APPPS1ΔE9 (133.2 ± 8.5, *n* = 7 mice) were not significantly different; t(16) = 1.4, P = 0.19, Student's *t* test. **(E)** Selected differentially expressed inflammatory gene expression from APP PS1 (*n* = 6 mice) and *Apoe*−/−;APPPS1 mice (*n* = 7 mice). See Table S1 for p-values. **(F)** Analysis of cytokine levels in the hippocampus of APPPS1 and *Apoe*−/−; APPPS1 mice. *Apoe*−/−;APPPS1 mice (*n* = 13 mice) exhibited a significant reduction in CCL3 compared with APPPS1 mice (*n* = 11 mice). P < 0.0001, Student's *t* test. Bars, 100 μm. ***, P < 0.001.

The influence of apoE on microglial activation may have important implications for apoE-modulating therapies in AD.

One limitation of the current study is that we did not examine the potential contribution of apoE-dependent vascular BBB changes on plaque deposition or the immune response. Previous studies indicate that *Apoe*−/− mice have age-dependent BBB dysfunction, which leads to extravasation of peripheral proteins with neurotoxic consequences (Hafezi-Moghadam et al., 2007; Bell et al., 2012). Moreover, a compromised BBB could lead to

increased infiltration of peripheral macrophages and neutrophils into the brain, which may also be neurotoxic (Zenaro et al., 2015). Conceivably, the increase in dystrophic neurites we observe in *Apoe*−/− could be promoted in part by infiltrating neutrophils or a compromised BBB. In addition, we cannot exclude the possibility that overexpression of APP and PS1 may also influence the phenotypes we report here. Future studies using APP knock-in mice that test whether Apoe-dependent alterations in the BBB affect microgliosis, plaque burden, and neuritic dystrophy could
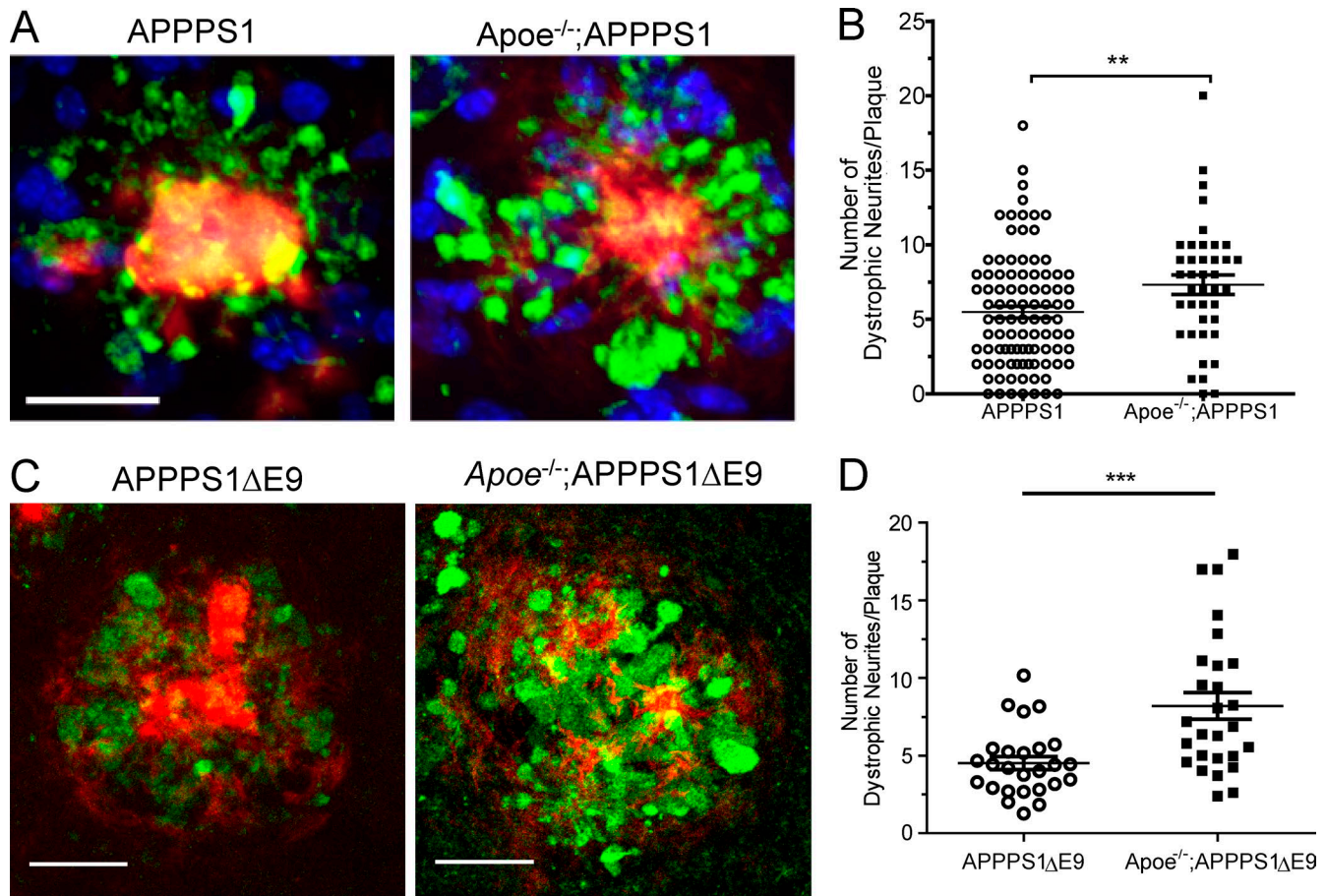
Figure 4.   Significant increase in plaque-associated neuritic dystrophy in *Apoe*-deficient mice. (A) Representative image of dystrophic neurites labeled with APP (green) and amyloid labeled with X-34 (red). Nuclei are labeled with Topro-3 (blue). **(B)** Significant increase in the number of dystrophic neurites per plaque in *Apoe*^{−/−};APPPS1 mice (7.3 ± 0.66, *n* = 40 plaques) compared with APPPS1 (5.5 ± 0.39, *n* = 95 plaques); t(133) = 2.48, P = 0.01, Student's *t* test. **(C)** Representative image of neuritic dystrophy in APPPS1ΔE9 and *Apoe*^{−/−};APPPS1ΔE9 mice. **(D)** Significant increase in the number of dystrophic neurites per plaque in *Apoe*^{−/−};APPPS1ΔE9 mice (8.2 ± 0.86, *n* = 27 plaques) compared with APPPS1ΔE9 (4.5 ± 0.42, *n* = 26 plaques); t(51) = 3.8, P = 0.0004, Student's *t* test. All values given and plotted as mean ± SEM. Bars, 20 µm. **, P < 0.01; ***, P < 0.001.

provide additional insight into potential mechanisms underlying our observations (Saito et al., 2014).

In addition to BBB dysfunction, *Apoe*^{−/−} mice develop hypercholesterolemia and atherosclerosis, which are accompanied by immune responses to atherosclerotic plaques (Zhou et al., 1996). Interestingly, the background strain can strongly influence the degree of atherosclerosis that develops in *Apoe*^{−/−} mice; C57BL/6 mice exhibit more robust atherosclerosis pathology than C3H mice (Su et al., 2006). We observed an increase in the number of Aβ-immunoreactive plaques in *Apoe*^{−/−};APPPS1 mice, which are on a C57BL/6 background, and a decrease in the number of Aβ-immunoreactive plaques in *Apoe*^{−/−};APPPS1ΔE9 mice, which are on a mixed C57BL/6;C3H background. Whether the degree of vascular pathology contributed to this dichotomous result is unknown, and it is important to note that in addition to background strain and PSEN1 mutations, the APPPS1 and APPPS1ΔE9 mice also differ in the promoter used for transgene expression (*Thy1* vs. *Prp*, respectively). Overall, the different effects of *Apoe*^{−/−} on Aβ burden we describe in APPPS1 and APPPS1ΔE9 suggest that the choice of Aβ-deposition model can strongly influence the effect of gene KO on Aβ pathology. It is important

to note that despite the differing effects on Aβ pathology, we observed consistent effects of *Apoe*-deficiency on fibrillar Aβ deposition, microgliosis, and neuritic dystrophy in both APPPS1 and APPPS1ΔE9 models.

ApoE expression is up-regulated in AD, which is generally attributed to a proinflammatory response to Aβ pathology. Within the brain, apoE is predominantly expressed by astrocytes, although microglia, particularly in an activated state, also produce apoE (Zhao et al., 2018). The relative contribution of microglial and astrocyte-derived apoE to the regulation of Aβ deposition and microgliosis is unclear. Microglia immunoreactive for apoE were noted to be intimately associated with senile plaques, in contrast to astrocytes, which were localized more distally to plaques. The proximity of microglia versus astrocytes to plaques could indicate a unique role for microglial expressed apoE in the immune response to AD pathology (Uchihara et al., 1995). Investigations into the effects of apoE on plaque-associated microgliosis have focused largely on apoE isoform–dependent effects. ApoE4 and apoE2 exhibited increased numbers of plaque-associated microglia within certain cortical regions of 5xFAD mice compared with apoE3 (Rodriguez et al., 2014).

However, the *APOE4* allele did not appear to affect the magnitude of plaque-associated microgliosis in human AD patients (Serrano-Pozo et al., 2013). ApoE expression in general has been shown to have pleiotropic effects on microglia and the broader immune response. ApoE expression is low in microglia in a homeostatic activation state, but is strongly up-regulated by neurodegenerative insults (Butovsky et al., 2014, 2015; Krasemann et al., 2017). Moreover, application of recombinant apoE to cultured microglia is sufficient to polarize gene expression away from a resting state toward a more activated phenotype (Butovsky et al., 2015). This suggests that apoE is a powerful modulator of microglial phenotype, in agreement with our current findings. In addition, the influence of apoE on microglial physiology does not appear to be specific to amyloid pathology. Reductions in microgliosis were also observed in the experimental autoimmune encephalomyelitis model of multiple sclerosis and reduced inflammation and neurodegeneration were observed in an *Apoe*-deficient model of tauopathy (Shin et al., 2014; Shi et al., 2017).

The function of plaque-associated microgliosis remains poorly understood. Some recent studies may indicate that microgliosis around plaques may initially have a neuroprotective role. Plaque-associated dystrophic neurites appear in areas devoid of microglial coverage, suggesting that microglia may limit amyloid toxicity in plaque-adjacent neurons (Condello et al., 2015). An alternative interpretation is that a reduction in plaque-associated microglia could hamper phagocytic clearance of injured dystrophic neurites, resulting in an apparent increase in neuritic dystrophy. ApoE isoforms can differentially influence the phagocytosis of synapses by astrocytes and the amount of C1q deposition in aging (Chung et al., 2016). Thus *Apoe* expression, either by astrocytes or microglia, may promote the clearance of damaged neurites around plaques. Future studies investigating cell type–specific expression of apoE or inhibition of apoE expression following plaque deposition could provide insight into the mechanistic basis by which apoE influences the innate immune response in the context of amyloid pathology.

Materials and methods

Mice
APPPS1-21 (APPPS1) transgenic mice on a C57BL6 background containing the APP KM670/671NL Swedish mutations and PSEN1 L166P mutation (gift from M. Jucke, University of Tübingen, Tübingen, Germany; Radde et al., 2006) were crossed with *Apoe*$^{-/-}$ mice on a C57BL6 background (Jackson Labs) to produce *Apoe*$^{+/-}$;APPPS1 mice. *Apoe*$^{+/-}$;APPPS1 mice were then bred with *Apoe*$^{+/+}$ or *Apoe*$^{-/-}$ mice to produce APPPS1 or APOE$^{-/-}$;APPPS1 mice. APPPS1ΔE9 (APPPS1;ΔE9) transgenic mice on a C3B6 background (Jackson Labs) containing the APP KM670/671NL Swedish mutations and PSEN1 exon 9 deletion were similarly crossed with *Apoe*$^{-/-}$ mice to produce *Apoe*$^{+/-}$;APPPS1ΔE9 mice. *Apoe*$^{+/-}$;APPPS1ΔE9 mice were then bred to either *Apoe*$^{-/-}$ or C57BL6 mice to produce *Apoe*$^{-/-}$;APPPS1ΔE9 or APPPS1ΔE9 mice on a mixed C57BL6;C3B6 background. APPPS1 mice were analyzed at 6 mo of age and APPPS1ΔE9 mice were analyzed at 10 mo of age. All experimental procedures relating to animal use were approved by the Washington University Institutional Animal Care and Use Committee.

Brain sample collection
Mice were anesthetized with intraperitoneal 200-mg/kg injections of pentobarbital and perfused with ice-cold PBS containing 0.3% Heparin. One hemibrain was fixed in 4% paraformaldehyde overnight at 4°C followed by storage in a 30% sucrose in PBS (pH 7.4) solution at 4°C. The other hemibrain was dissected and flash frozen for further analysis and stored at –80°C.

Histological analysis
Fixed hemibrains were frozen and serial 50-μm coronal sections were obtained from the rostral to caudal end using a sliding microtome. Sections were stored in a cryoprotectant solution (30% ethylene glycol, 15% sucrose, and 30 mM phosphate) and stored at –20°C. Three 50-μm sections spaced 300 μm apart were used for each staining procedure.

Amyloid plaque staining and morphology
To visualize Aβ plaques, APPPS1 and *Apoe*$^{-/-}$;APPPS1 mice were immunostained using the anti-Aβ$_{1-5}$ antibody 3D6 (gift from Eli Lilly, Lilly Corporate Center, Indianapolis, IN), whereas immunostaining for APPPS1ΔE9 and *Apoe*$^{-/-}$;APPPS1ΔE9 mice was performed with the anti-Aβ$_{1-13}$ antibody HJ3.4. All sections were free-floating and were first treated with 0.3% hydrogen peroxide, blocked in 3% milk + 0.25% Triton X-100 in Tris-buffered saline (TBS), and then incubated overnight in biotinylated 3D6 or HJ3.4 accordingly at 4°C. Sections were then developed using a Vectastain ABC Elite kit (1:400; Vector Labs), followed by incubation in a 0.025% 3,3′-diaminobenzidine (DAB; Sigma-Aldrich) + 0.01% NiCl + 0.015% hydrogen peroxide solution. Images of the stained sections were obtained using a slide scanner (Nano-Zoomer; Hamamatsu Photonics), exported using NDP Viewer (Hamamatsu Photonics), and analyzed using ImageJ software (National Institutes of Health). To identify fibrillar plaques, free-floating sections from the APPPS1, *Apoe*$^{-/-}$;APPPS1, APPPS1ΔE9, and *Apoe*$^{-/-}$;APPPS1ΔE9 mice were all permeabilized with 0.25% Triton X-100 in PBS and stained with 10 μM X-34 in 40% ethanol + 0.02M NaOH in PBS. X-34 images were obtained with an Eclipse 80i microscope (Nikon) equipped with a digital complementary metal-oxide semiconductor camera (ORCA-Flash4.0 V2; Hamamatsu Photonics) and analyzed using ImageJ software to determine fibrillar plaque levels.

To determine fibrillar plaque morphology, z-stacked images were taken every 0.75 μm from X-34–stained sections. Images were acquired on a confocal microscope (A1R+; Nikon) at 40× magnification with 1.5× digital zoom. Max intensity projections of the z-stack images were then used to assess shape compactness, average intensity, and intensity Gini coefficient. A blurring filter was first applied to images to clarify the plaque from background. All pixels >2× background were considered part of the plaque, whereas pixels <1.5× background were considered nonplaque. Pixels between 1.5 and 2× backgrounds were assigned based on edge detection. Average intensity was determined based on plaque pixels. Gini coefficient was based on the distribution of pixel intensity for plaque pixels. Shape compactness was

determined as the ratio of plaque area pixels to plaque perimeter pixels after scaling plaques to be the same overall area.

Aβ ELISA
Cortical tissues from 6-mo-old APPPS1 and $Apoe^{-/-}$;APPPS1 mice were hand-homogenized in 10-fold volume PBS using a Teflon pestle. Brain homogenates were spun at 14,000 g for 30 min, and the supernatant was retained as the soluble fraction. The pellet was resuspended in 10-fold volume 5 M guanidine, hand homogenized, and rotated for 3 h at room temperature. Homogenates were clarified by centrifugation at 14,000 g for 30 min, and the supernatant was retained as the insoluble fraction. $Aβ_{40}$ and $Aβ_{42}$ concentrations were measured by sandwich ELISA. $Aβ_{40}$ concentration was measured using HJ2 as the capture antibody and biotinylated HJ5.1 as the detection antibody. $Aβ_{42}$ was measured using HJ7.4 as the capture antibody and biotinylated HJ5.1 as the detection antibody. ELISAs were developed using streptavidin-PolyHRP40 (Fitzgerald) and TMB Superslow reagent (Sigma Aldrich). $Aβ_{40}$ and $Aβ_{42}$ values were normalized to wet weight of brain tissue.

Western blotting
Hippocampal tissue was homogenized in 10-fold volume lysis buffer (10 mM Tris-HCl, pH 8.0, 1 mM EDTA, 1% Triton X-100, 0.1% SDS, and 150 mM NaCl), and lysate was clarified by centrifugation at 15,000 g at 4°C. Total protein concentrations in lysate were quantified using a BCA assay, and 50 µg of protein were loaded onto a 4–20% Bis-Tris SDS-PAGE gel followed by transfer to nitrocellulose. Full-length APP was detected using 6E10 (1:1,000; Biolegend), and C99 fragment was detected using 82E1 (1:1,000; IBL America). Protein detection was visualized using an HRP-coupled anti–mouse secondary antibody (1:5,000) and ECL reagent. Images of the blot were captured using a G Box (SynGene) and analyzed in ImageJ.

Cytokine assessment
Levels of IL1β, IL-10, TNF-α, CCL3, CCL2, and CCL4 were assessed using a Milliplex multianalyte profiling kit (Millipore) per the manufacturer's instructions. Assays were run on a FlexMAP 3D (Luminex) at the Andrew M. and Jane M. Bursky Center for Human Immunology & Immunotherapy Programs at Washington University, St. Louis, MO. Cytokine levels were normalized for total protein content in lysate as calculated by BCA assay.

LCO staining and fluorescence microscopy
The synthesis of the LCOs, q-FTAA, and h-FTAA have been reported previously (Klingstedt et al., 2011), and the LCOs were dissolved in deionized water to a final concentration of 1.5 mM. Floating sections from 6-mo-old APPPS1 or $Apoe^{-/-}$;APPPS1 mice were equilibrated in PBS and stained with a mixture of 2.4 µM q-FTAA and 0.77 µM h-FTAA in PBS or 0.77 µM h-FTAA in PBS for 30 min (Nyström et al., 2013). After washing in incubation buffer the sections were transferred to glass slides and mounted with mounting media (DAKO; Agilent). The mounting medium was allowed to solidify overnight before the rims were sealed with nail polish. The LCO-stained sections were analyzed with a confocal laser scanning microscope (LSM 780; Zeiss) equipped with a 32-channel spectral array detector (QUASAR GaAsP; Zeiss) and a tunable In Tune laser (488–640 nm; Zeiss), as well as a modular FLIM system (Becker and Hickl). In spectral mode, q-FTAA and h-FTAA were excited with a 458-nm laser, and the emitted light was detected in steps of 8.7 nm from 488 to 686 nm. Z-stacks were recorded with the dimension of x = 250 µm, y = 250 µm, and z = 90 µm using a Plan-Apochromat 20×/0.8 M27, and three-dimensional images were generated by spectral mixing using the ZEN2010 software. Three-dimensional images were rendered by spectral unmixing using the ZEN2010 software. For the FLIM, the emitted photons were routed through the direct coupling confocal port of a scanning unit (LSM 780; Zeiss) and detected by a hybrid detector (HPM-100-40; Becker and Hickl). Data were recorded by a Simple-Tau 152 system (SPC-150 TCSPC FLIM module; Becker and Hickl) with the instrument recording software SPCM version 9.42 (Becker and Hickl) in the FIFO image mode, 256 × 256 pixels, using 256 time channels (Becker and Hickl). For all acquisitions, a main beam splitter (T80/R20; Zeiss) was used and the pinhole was set to 20.2 µm. Scanning area was set to 235.7 × 235.7 µm, with a scanning resolution of 512 × 512 pixels. Furthermore, a Plan-Apochromat 40×/1.3 Oil DIC objective lens was used, and a 510-nm long pass filter was positioned in front of the hybrid PMT. Excitation used the 490-nm laser line from the pulsed tunable In Tune laser with a repetition rate of 40 MHz. Data were subsequently analyzed in SPCImage version 3.9.4 (Becker and Hickl), fitting each of the acquired decay curves to a triexponential function, and color-coded images showing the intensity-weighted mean lifetimes were generated with the same software. Fluorescence decays were collected from 5–10 different plaques in tissue sections from five individual 6-mo-old APPPS1 or $Apoe^{-/-}$;APPPS1 mice.

Microglia, dystrophic neurites, and fibrillar plaque staining
To assess microglial colocalization with fibrillar plaques, sections from each group of mice were costained with X-34 and Iba-1. Free-floating sections were first stained with X-34 followed by blocking, using 3% normal donkey serum in TBS and then incubation with rabbit anti–Iba-1 (1:10,000; Wako) + 1% donkey serum in TBS overnight at 4°C. Iba-1–stained sections were then incubated in secondary donkey anti–rabbit Alexa Fluor 647 (1:1000; Thermo Fisher) in PBS. Neuritic dystrophy around fibrillar plaques was assessed in each group of mice using 22C11, an antibody to the N terminus of APP, and the X-34 dye. Free-floating sections were blocked in confocal buffer (0.5% BSA, 2% goat serum, and 0.15% Triton X-100 in PBS) and then incubated with 22C11 (1:2,000; Millipore) in confocal buffer overnight at 4°C. Sections were then incubated in confocal buffer with biotinylated goat anti–mouse IgG1 (1:2,000; Thermo Fisher) followed by Streptavidin-488 (1:2,000; Thermo Fisher) + To-Pro3 (nuclear stain, 1:1,000; Thermo Fisher) in PBS.

Confocal analysis
Confocal images were taken in the cortical regions of the Iba-1/X-34– and APP/X-34–stained sections using a confocal microscope (A1R+; Nikon). Z-stacked images were acquired every 1.25 µm at a 20× magnification. Images were then analyzed using Imaris software (Bitplane) or ImageJ. For all Imaris analyses,

Ulrich et al.
ApoE and microglia activation in amyloid models

Journal of Experimental Medicine
1055
https://doi.org/10.1084/jem.20171265

the Spots and Surfaces functions were used. The coordinates of microglia and the location and volume of Aβ plaques were identified using the Spots and Surfaces functions, respectively, and imported into Matlab (Mathworks). The number of microglia within a 15- and 30-μm radius were then determined using an automated script. The level of APP accumulation in neuritic processes surrounding X-34 plaques for APPPS1 and $Apoe^{-/-}$; APPPS1 mice was determined by creating Spots for APP and Surfaces for X-34. The volume and number of APP-NT+ neuritic processes was determined within 30 μm using an automated script. For APPPS1ΔE9 and $Apoe^{-/-}$;APPPS1ΔE9 mice the level of APP around X-34 plaques was determined by creating surfaces for both APP and X-34. The Dilate Xtension was used to dilate out the X-34 plaque surface 15 μm and create a second dilated surface. To determine the volume of APP surface within 15 μm of X-34 plaque, surface–surface colocalization Xtension was run using the dilated surface and APP surface as the two surfaces for comparison. The number and volume of APP-NT+ neurites per plaque was found and determined based on overall X-34 plaque volume.

RNAseq analysis
RNA was extracted from frozen cortex tissue of 6-mo-old APPPS1 and $Apoe^{-/-}$;APPPS1 mice using TRIzol per the manufacturer's instructions. Isolated RNA was then treated with DNase to remove any contaminating genomic DNA and RNA integrity assessed using a Bioanalyzer 2100 (Agilent) to ensure an RNA integrity number >7. Library preparation was performed using the SMARTer RNA kit (Clontech), and libraries were sequenced on a HiSeq2500. Sequence data were aligned to the mouse reference genome mm10 using STAR. Gene-level differential expression analysis was performed in Partek Genomic Suite. Gene ontology enrichment analysis was performed in Partek Genomic Suite by comparing the list of differentially expressed genes with the gene ontology database using a Fisher's exact test. All data have been deposited at GEO (accession no. GSE109906).

Statistical analysis
Statistical significance between two groups was assessed by two-tailed, unpaired Student's t test with significance assigned for $P < 0.05$. Statistical analysis of differential gene expression from RNAseq data were assessed using Partek Genomic Suite. A corrected p-value of 0.05 following Benjamini-Hochberg correction for multiple comparisons was considered statistically significant.

Online supplemental material
Fig. S1 shows that 6-mo-old $Apoe^{-/-}$;APPPS1 mice exhibit reduced insoluble levels of Aβ$_{40}$ and Aβ$_{42}$ compared with APPPS1 mice. Table S1 presents the list of genes that were differentially expressed in the cortex of 6-mo-old $Apoe^{-/-}$;APPPS1 and APPPS1 mice with a $P < 0.05$ following false discovery rate correction. Table S2 presents the top 10 gene ontology functions identified for differentially expressed genes in $Apoe^{-/-}$;APPPS1 and APPPS1 mice.

References
Aguzzi, A., B.A. Barres, and M.L. Bennett. 2013. Microglia: scapegoat, saboteur, or something else? *Science.* 339:156–161. https://doi.org/10.1126/science.1227901

Atagi, Y., C.-C. Liu, M.M. Painter, X.-F. Chen, C. Verbeeck, H. Zheng, X. Li, R. Rademakers, S.S. Kang, H. Xu, et al. 2015. Apolipoprotein E Is a Ligand for Triggering Receptor Expressed on Myeloid Cells 2 (TREM2). *J. Biol. Chem.* 290:26043–26050. https://doi.org/10.1074/jbc.M115.679043

Bales, K.R., T. Verina, R.C. Dodel, Y. Du, L. Altstiel, M. Bender, P. Hyslop, E.M. Johnstone, S.P. Little, D.J. Cummins, et al. 1997. Lack of apolipoprotein E dramatically reduces amyloid beta-peptide deposition. *Nat. Genet.* 17:263–264. https://doi.org/10.1038/ng1197-263

Bales, K.R., T. Verina, D.J. Cummins, Y. Du, R.C. Dodel, J. Saura, C.E. Fishman, C.A. DeLong, P. Piccardo, V. Petegnief, et al. 1999. Apolipoprotein E is essential for amyloid deposition in the APP(V717F) transgenic mouse model of Alzheimer's disease. *Proc. Natl. Acad. Sci. USA.* 96:15233–15238. https://doi.org/10.1073/pnas.96.26.15233

Bell, R.D., A.P. Sagare, A.E. Friedman, G.S. Bedi, D.M. Holtzman, R. Deane, and B.V. Zlokovic. 2007. Transport pathways for clearance of human Alzheimer's amyloid β-peptide and apolipoproteins E and J in the mouse central nervous system. *J. Cereb. Blood Flow Metab.* 27:909–918. https://doi.org/10.1038/sj.jcbfm.9600419

Bell, R.D., E.A. Winkler, I. Singh, A.P. Sagare, R. Deane, Z. Wu, D.M. Holtzman, C. Betsholtz, A. Armulik, J. Sallstrom, et al. 2012. Apolipoprotein E controls cerebrovascular integrity via cyclophilin A. *Nature.* 485:512–516. https://doi.org/10.1038/nature11087

Butovsky, O., M.P. Jedrychowski, C.S. Moore, R. Cialic, A.J. Lanser, G. Gabriely, T. Koeglsperger, B. Dake, P.M. Wu, C.E. Doykan, et al. 2014. Identification of a unique TGF-β-dependent molecular and functional signature in microglia. *Nat. Neurosci.* 17:131–143. https://doi.org/10.1038/nn.3599

Butovsky, O., M.P. Jedrychowski, R. Cialic, S. Krasemann, G. Murugaiyan, Z. Fanek, D.J. Greco, P.M. Wu, C.E. Doykan, O. Kiner, et al. 2015. Targeting miR-155 restores abnormal microglia and attenuates disease in SOD1 mice. *Ann. Neurol.* 77:75–99. https://doi.org/10.1002/ana.24304

Chung, W.-S., P.B. Verghese, C. Chakraborty, J. Joung, B.T. Hyman, J.D. Ulrich, D.M. Holtzman, and B.A. Barres. 2016. Novel allele-dependent role for APOE in controlling the rate of synapse pruning by astrocytes. *Proc. Natl. Acad. Sci. USA.* 113:10186–10191. https://doi.org/10.1073/pnas.1609896113

Condello, C., P. Yuan, A. Schain, and J. Grutzendler. 2015. Microglia constitute a barrier that prevents neurotoxic protofibrillar Aβ42 hotspots around plaques. *Nat. Commun.* 6:6176. https://doi.org/10.1038/ncomms7176

Deane, R., A. Sagare, K. Hamm, M. Parisi, S. Lane, M.B. Finn, D.M. Holtzman, and B.V. Zlokovic. 2008. apoE isoform-specific disruption of amyloid β peptide clearance from mouse brain. *J. Clin. Invest.* 118:4002–4013. https://doi.org/10.1172/JCI36663

Fagan, A.M., M. Watson, M. Parsadanian, K.R. Bales, S.M. Paul, and D.M. Holtzman. 2002. Human and murine ApoE markedly alters Aβ metabolism before and after plaque formation in a mouse model of Alzheimer's disease. *Neurobiol. Dis.* 9:305–318. https://doi.org/10.1006/nbdi.2002.0483

Grainger, D.J., J. Reckless, and E. McKilligin. 2004. Apolipoprotein E modulates clearance of apoptotic bodies in vitro and in vivo, resulting in a systemic proinflammatory state in apolipoprotein E-deficient mice. *J. Immunol.* 173:6366–6375. https://doi.org/10.4049/jimmunol.173.10.6366

Griciuc, A., A. Serrano-Pozo, A.R. Parrado, A.N. Lesinski, C.N. Asselin, K. Mullin, B. Hooli, S.H. Choi, B.T. Hyman, and R.E. Tanzi. 2013. Alzheimer's disease risk gene CD33 inhibits microglial uptake of amyloid beta. *Neuron.* 78:631–643. https://doi.org/10.1016/j.neuron.2013.04.014

Guerreiro, R., A. Wojtas, J. Bras, M. Carrasquillo, E. Rogaeva, E. Majounie, C. Cruchaga, C. Sassi, J.S.K. Kauwe, S. Younkin, et al. Alzheimer Genetic Analysis Group. 2013. TREM2 variants in Alzheimer's disease. *N. Engl. J. Med.* 368:117–127. https://doi.org/10.1056/NEJMoa1211851

Gutierrez, E.G., W.A. Banks, and A.J. Kastin. 1993. Murine tumor necrosis factor alpha is transported from blood to brain in the mouse. *J. Neuroimmunol.* 47:169–176. https://doi.org/10.1016/0165-5728(93)90027-V

Hafezi-Moghadam, A., K.L. Thomas, and D.D. Wagner. 2007. ApoE deficiency leads to a progressive age-dependent blood-brain barrier leakage. *Am. J. Physiol. Cell Physiol.* 292:C1256–C1262. https://doi.org/10.1152/ajpcell.00563.2005

Heneka, M.T., D.T. Golenbock, and E. Latz. 2015. Innate immunity in Alzheimer's disease. *Nat. Immunol.* 16:229–236. https://doi.org/10.1038/ni.3102

Holtzman, D.M., K.R. Bales, S. Wu, P. Bhat, M. Parsadanian, A.M. Fagan, L.K. Chang, Y. Sun, and S.M. Paul. 1999. Expression of human apolipoprotein E reduces amyloid-β deposition in a mouse model of Alzheimer's disease. *J. Clin. Invest.* 103:R15–R21. https://doi.org/10.1172/JCI6179

Holtzman, D.M., A.M. Fagan, B. Mackey, T. Tenkova, L. Sartorius, S.M. Paul, K. Bales, K.H. Ashe, M.C. Irizarry, and B.T. Hyman. 2000. Apolipoprotein E facilitates neuritic and cerebrovascular plaque formation in an Alzheimer's disease model. *Ann. Neurol.* 47:739–747.

Huynh, T.V., A.A. Davis, J.D. Ulrich, and D.M. Holtzman. 2017a. Apolipoprotein E and Alzheimer's disease: The influence of apolipoprotein E on amyloid-β and other amyloidogenic proteins. *J. Lipid Res.* 58:824–836. https://doi.org/10.1194/jlr.R075481

Huynh, T.V., F. Liao, C.M. Francis, G.O. Robinson, J.R. Serrano, H. Jiang, J. Roh, M.B. Finn, P.M. Sullivan, T.J. Esparza, et al. 2017b. Age-Dependent Effects of apoE Reduction Using Antisense Oligonucleotides in a Model of β-amyloidosis. *Neuron.* 96:1013–1023.e4. https://doi.org/10.1016/j.neuron.2017.11.014

Irizarry, M.C., B.S. Cheung, G.W. Rebeck, S.M. Paul, K.R. Bales, and B.T. Hyman. 2000. Apolipoprotein E affects the amount, form, and anatomical distribution of amyloid beta-peptide deposition in homozygous APP(V717F) transgenic mice. *Acta Neuropathol.* 100:451–458. https://doi.org/10.1007/s004010000263

Jankowsky, J.L., D.J. Fadale, J. Anderson, G.M. Xu, V. Gonzales, N.A. Jenkins, N.G. Copeland, M.K. Lee, L.H. Younkin, S.L. Wagner, et al. 2004. Mutant presenilins specifically elevate the levels of the 42 residue β-amyloid peptide in vivo: evidence for augmentation of a 42-specific γ secretase. *Hum. Mol. Genet.* 13:159–170. https://doi.org/10.1093/hmg/ddh019

Jay, T.R., A.M. Hirsch, M.L. Broihier, C.M. Miller, L.E. Neilson, R.M. Ransohoff, B.T. Lamb, and G.E. Landreth. 2017. Disease progression-dependent effects of TREM2 deficiency in a mouse model of Alzheimer's disease. *J. Neurosci.* 37:637–647. https://doi.org/10.1523/JNEUROSCI.2110-16.2016

Jonsson, T., H. Stefansson, S. Steinberg, I. Jonsdottir, P.V. Jonsson, J. Snaedal, S. Bjornsson, J. Huttenlocher, A.I. Levey, J.J. Lah, et al. 2013. Variant of TREM2 associated with the risk of Alzheimer's disease. *N. Engl. J. Med.* 368:107–116. https://doi.org/10.1056/NEJMoa1211103

Katsouri, L., and S. Georgopoulos. 2011. Lack of LDL receptor enhances amyloid deposition and decreases glial response in an Alzheimer's disease mouse model. *PLoS One.* 6:e21880. https://doi.org/10.1371/journal.pone.0021880

Keren-Shaul, H., A. Spinrad, A. Weiner, O. Matcovitch-Natan, R. Dvir-Szternfeld, T.K. Ulland, E. David, K. Baruch, D. Lara-Astaiso, B. Toth, et al. 2017. A Unique Microglia Type Associated with Restricting Development of Alzheimer's Disease. *Cell.* 169:1276–1290.e17. https://doi.org/10.1016/j.cell.2017.05.018

Klingstedt, T., A. Aslund, R.A. Simon, L.B.G. Johansson, J.J. Mason, S. Nyström, P. Hammarström, and K.P.R. Nilsson. 2011. Synthesis of a library of oligothiophenes and their utilization as fluorescent ligands for spectral assignment of protein aggregates. *Org. Biomol. Chem.* 9:8356–8370. https://doi.org/10.1039/c1ob05637a

Klingstedt, T., C. Blechschmidt, A. Nogalska, S. Prokop, B. Häggqvist, O. Danielsson, W.K. Engel, V. Askanas, F.L. Heppner, and K.P.R. Nilsson. 2013. Luminescent conjugated oligothiophenes for sensitive fluorescent assignment of protein inclusion bodies. *ChemBioChem.* 14:607–616. https://doi.org/10.1002/cbic.201200731

Krasemann, S., C. Madore, R. Cialic, C. Baufeld, N. Calcagno, R. El Fatimy, L. Beckers, E. O'Loughlin, Y. Xu, Z. Fanek, et al. 2017. The TREM2-APOE Pathway Drives the Transcriptional Phenotype of Dysfunctional Microglia in Neurodegenerative Diseases. *Immunity.* 47:566–581.e9. https://doi.org/10.1016/j.immuni.2017.08.008

Liu, C.-C., N. Zhao, Y. Fu, N. Wang, C. Linares, C.-W. Tsai, and G. Bu. 2017. ApoE4 Accelerates Early Seeding of Amyloid Pathology. *Neuron.* 96:1024–1032.e3. https://doi.org/10.1016/j.neuron.2017.11.013

Magnusson, K., R. Simon, D. Sjölander, C.J. Sigurdson, P. Hammarström, and K.P.R. Nilsson. 2014. Multimodal fluorescence microscopy of prion strain specific PrP deposits stained by thiophene-based amyloid ligands. *Prion.* 8:319–329. https://doi.org/10.4161/pri.29239

Mauch, D.H., K. Nägler, S. Schumacher, C. Göritz, E.-C. Müller, A. Otto, and F.W. Pfrieger. 2001. CNS synaptogenesis promoted by glia-derived cholesterol. *Science.* 294:1354–1357. https://doi.org/10.1126/science.294.5545.1354

Musiek, E.S., and D.M. Holtzman. 2015. Three dimensions of the amyloid hypothesis: time, space and 'wingmen'. *Nat. Neurosci.* 18:800–806. https://doi.org/10.1038/nn.4018

Naj, A.C., G. Jun, G.W. Beecham, L.-S. Wang, B.N. Vardarajan, J. Buros, P.J. Gallins, J.D. Buxbaum, G.P. Jarvik, P.K. Crane, et al. 2011. Common variants at MS4A4/MS4A6E, CD2AP, CD33 and EPHA1 are associated with late-onset Alzheimer's disease. *Nat. Genet.* 43:436–441. https://doi.org/10.1038/ng.801

Nyström, S., K.M. Psonka-Antonczyk, P.G. Ellingsen, L.B.G. Johansson, N. Reitan, S. Handrick, S. Prokop, F.L. Heppner, B.M. Wegenast-Braun, M. Jucker, et al. 2013. Evidence for age-dependent in vivo conformational rearrangement within Aβ amyloid deposits. *ACS Chem. Biol.* 8:1128–1133. https://doi.org/10.1021/cb4000376

Radde, R., T. Bolmont, S.A. Kaeser, J. Coomaraswamy, D. Lindau, L. Stoltze, M.E. Calhoun, F. Jäggi, H. Wolburg, S. Gengler, et al. 2006. Abeta42-driven cerebral amyloidosis in transgenic mice reveals early and robust pathology. *EMBO Rep.* 7:940–946. https://doi.org/10.1038/sj.embor.7400784

Rodriguez, G.A., L.M. Tai, M.J. LaDu, and G.W. Rebeck. 2014. Human APOE4 increases microglia reactivity at Aβ plaques in a mouse model of Aβ deposition. *J. Neuroinflammation.* 11:111. https://doi.org/10.1186/1742-2094-11-111

Saito, T., Y. Matsuba, N. Mihira, J. Takano, P. Nilsson, S. Itohara, N. Iwata, and T.C. Saido. 2014. Single App knock-in mouse models of Alzheimer's disease. *Nat. Neurosci.* 17:661–663. https://doi.org/10.1038/nn.3697

Serrano-Pozo, A., A. Muzikansky, T. Gómez-Isla, J.H. Growdon, R.A. Betensky, M.P. Frosch, and B.T. Hyman. 2013. Differential relationships of reactive astrocytes and microglia to fibrillar amyloid deposits in Alzheimer disease. *J. Neuropathol. Exp. Neurol.* 72:462–471. https://doi.org/10.1097/NEN.0b013e3182933788

Shi, Y., K. Yamada, S.A. Liddelow, S.T. Smith, L. Zhao, W. Luo, R.M. Tsai, S. Spina, L.T. Grinberg, J.C. Rojas, et al. 2017. ApoE4 markedly exacerbates tau-mediated neurodegeneration in a mouse model of tauopathy. *Nature.* 549:523–527. https://doi.org/10.1038/nature24016

Shin, S., K.A. Walz, A.S. Archambault, J. Sim, B.P. Bollman, J. Koenigsknecht-Talboo, A.H. Cross, D.M. Holtzman, and G.F. Wu. 2014. Apolipoprotein E mediation of neuro-inflammation in a murine model of multiple sclerosis. *J. Neuroimmunol.* 271:8–17. https://doi.org/10.1016/j.jneuroim.2014.03.010

Song, W., B. Hooli, K. Mullin, S.C. Jin, M. Cella, T.K. Ulland, Y. Wang, R. Tanzi, and M. Colonna. 2017. Alzheimer's disease-associated TREM2 variants exhibit either decreased or increased ligand-dependent activation. *Alzheimers Dement.* 13:381–387. https://doi.org/10.1016/j.jalz.2016.07.004

Srinivasan, K., B.A. Friedman, J.L. Larson, B.E. Lauffer, L.D. Goldstein, L.L. Appling, J. Borneo, C. Poon, T. Ho, F. Cai, et al. 2016. Untangling the brain's neuroinflammatory and neurodegenerative transcriptional responses. *Nat. Commun.* 7:11295. https://doi.org/10.1038/ncomms11295

Styren, S.D., R.L. Hamilton, G.C. Styren, and W.E. Klunk. 2000. X-34, a fluorescent derivative of Congo red: a novel histochemical stain for Alzheimer's disease pathology. *J. Histochem. Cytochem.* 48:1223–1232. https://doi.org/10.1177/002215540004800906

Su, Z., Y. Li, J.C. James, M. McDuffie, A.H. Matsumoto, G.A. Helm, J.L. Weber, A.J. Lusis, and W. Shi. 2006. Quantitative trait locus analysis of atherosclerosis in an intercross between C57BL/6 and C3H mice carrying the

mutant apolipoprotein E gene. *Genetics.* 172:1799–1807. https://doi.org/10.1534/genetics.105.051912

Uchihara, T., C. Duyckaerts, Y. He, K. Kobayashi, D. Seilhean, P. Amouyel, and J.-J. Hauw. 1995. ApoE immunoreactivity and microglial cells in Alzheimer's disease brain. *Neurosci. Lett.* 195:5–8. https://doi.org/10.1016/0304-3940(95)11763-M

Ulland, T.K., W.M. Song, S.C. Huang, J.D. Ulrich, A. Sergushichev, W.L. Beatty, A.A. Loboda, Y. Zhou, N.J. Cairns, A. Kambal, et al. 2017. TREM2 Maintains Microglial Metabolic Fitness in Alzheimer's Disease. *Cell.* 170:649–663.e13. https://doi.org/10.1016/j.cell.2017.07.023

Ulrich, J.D., M.B. Finn, Y. Wang, A. Shen, T.E. Mahan, H. Jiang, F.R. Stewart, L. Piccio, M. Colonna, and D.M. Holtzman. 2014. Altered microglial response to Aβ plaques in APPPS1-21 mice heterozygous for TREM2. *Mol. Neurodegener.* 9:20. https://doi.org/10.1186/1750-1326-9-20

Wang, Y., M. Cella, K. Mallinson, J.D. Ulrich, K.L. Young, M.L. Robinette, S. Gilfillan, G.M. Krishnan, S. Sudhakar, B.H. Zinselmeyer, et al. 2015. TREM2 lipid sensing sustains the microglial response in an Alzheimer's disease model. *Cell.* 160:1061–1071. https://doi.org/10.1016/j.cell.2015.01.049

Wang, Y., T.K. Ulland, J.D. Ulrich, W. Song, J.A. Tzaferis, J.T. Hole, P. Yuan, T.E. Mahan, Y. Shi, S. Gilfillan, et al. 2016. TREM2-mediated early microglial response limits diffusion and toxicity of amyloid plaques. *J. Exp. Med.* 213:667–675. https://doi.org/10.1084/jem.20151948

Yeh, F.L., Y. Wang, I. Tom, L.C. Gonzalez, and M. Sheng. 2016. TREM2 Binds to Apolipoproteins, Including APOE and CLU/APOJ, and Thereby Facilitates Uptake of Amyloid-Beta by Microglia. *Neuron.* 91:328–340. https://doi.org/10.1016/j.neuron.2016.06.015

Yuan, P., C. Condello, C.D. Keene, Y. Wang, T.D. Bird, S.M. Paul, W. Luo, M. Colonna, D. Baddeley, and J. Grutzendler. 2016. TREM2 Haplodeficiency in Mice and Humans Impairs the Microglia Barrier Function Leading to Decreased Amyloid Compaction and Severe Axonal Dystrophy. *Neuron.* 90:724–739. https://doi.org/10.1016/j.neuron.2016.05.003

Zenaro, E., E. Pietronigro, V. Della Bianca, G. Piacentino, L. Marongiu, S. Budui, E. Turano, B. Rossi, S. Angiari, S. Dusi, et al. 2015. Neutrophils promote Alzheimer's disease-like pathology and cognitive decline via LFA-1 integrin. *Nat. Med.* 21:880–886. https://doi.org/10.1038/nm.3913

Zhao, N., C.-C. Liu, W. Qiao, and G. Bu. 2018. Apolipoprotein E, Receptors, and Modulation of Alzheimer's Disease. *Biol. Psychiatry.* 83:347–357. https://doi.org/10.1016/j.biopsych.2017.03.003

Zhou, X., S. Stemme, and G.K. Hansson. 1996. Evidence for a local immune response in atherosclerosis. CD4+ T cells infiltrate lesions of apolipoprotein-E-deficient mice. *Am. J. Pathol.* 149:359–366.